Autonomous Navigation of a Lunar Relay Using GNSS and Other Measurements

Benjamin W. Ashman, *NASA Goddard Space Flight Center*
Luke B. Winternitz, *NASA Goddard Space Flight Center*
Nathan I. Stacey, *NASA Goddard Space Flight Center*
Anne C. Long, *a.i. solutions, Inc.*
Michael C. Schmidt, *a.i. solutions, Inc.*
Grant A. Ryden, *NASA Goddard Space Flight Center*
Andrew J. Liounis, *NASA Goddard Space Flight Center*
Samuel R. Price, *NASA Goddard Space Flight Center*
William A. Bamford, *Relative Dynamics, Inc.*
Sun H. Hur-Diaz, *NASA Goddard Space Flight Center*
Munther A. Hassouneh, *NASA Goddard Space Flight Center*
Liam A. Greenlee, *Aurora Engineering*

Biographies

Benjamin Ashman is a navigation engineer in the Navigation and Mission Design Branch at NASA Goddard Space Flight Center (GSFC) and was the 2021–2022 ION/AAAS Congressional Science and Engineering Fellow. He is the LCRNS PNT Instrument (LPI) Principal Investigator (PI).

Luke Winternitz is a navigation engineer working in NASA Goddard Space Flight Center's Components and Hardware Systems Branch since 2001. His work focuses on space GNSS receiver and navigation software development, testing, and analysis. He was the recipient of the 2017 ION Burka Award and 2023 ION Tycho Brahe Award.

Nathan Stacey is a navigation engineer in the Navigation and Mission Design Branch at NASA GSFC. He is the GEONS deputy product development lead, and he serves as a navigation subject matter expert for the autoNGC technology development project. Nathan is also an adjunct faculty member in the Johns Hopkins Applied Physics program.

Anne Long is a senior navigation engineer at a.i.i solutions, Inc. supporting the Navigation and Mission Design Branch at NASA GSFC in the investigation of lunar PNT performance.

Michael Schmidt is a flight dynamics engineer supporting the Navigation and Mission Design Branch at NASA GFSC. Michael provides support in tool development and analysis work for the LCRNS constellation design and navigation efforts.

Grant Ryden is a systems engineer in the Instrument/Payload Systems Engineering Branch at NASA GSFC. He is the LPI Instrument Systems Engineer.

Andrew Liounis is a navigation engineer in the Navigation and Mission Design Branch at NASA/GSFC. He serves as the optical navigation product design lead, the LuNaMaps project manager, and subject matter expert to numerous other projects including autoNGC.

Samuel Price is a navigation engineer in the Components and Hardware Systems Branch at NASA GSFC, where he specializes in space technology, including the development of navigation systems and hardware.

William Bamford is a navigation engineer at Relative Dynamics, Inc. supporting the Components and Hardware Systems Branch at NASA GSFC in the investigation of lunar PNT performance.

Sun Hur-Diaz is a navigation, guidance, and control engineer in the Navigation and Mission Design Branch at NASA GSFC. She is the Principal Investigator of the autoNGC technology development project.

Munther Hassouneh is a senior engineer in the Components and Hardware Systems branch at NASA GSFC. He leads the development of the NavCube3-mini lunar GNSS receiver and the GPS receiver for the PNT instrument.

Liam Greenlee is a flight software engineer supporting the Navigation and Mission Design Branch at NASA GSFC for the development and testing of autoNGC.

Abstract

NASA's Lunar Communications Relay and Navigation Services (LCRNS) project will establish a relay constellation at the Moon to provide the south pole region with communications and position, navigation, and time (PNT) services. These services will require highly accurate knowledge of position, velocity, and time (PVT) for each relay. This paper explores one approach for performing onboard PVT estimation, the LCRNS PNT Instrument (LPI). This paper considers different configurations of the instrument, specifically different measurement types and clocks, and the resulting navigation performance. Simulation results are first shown for an instrument configuration that uses GPS pseudorange and Doppler measurements with a highly sensitive GPS receiver (i.e., an acquisition and tracking threshold of 23 dB-Hz) and a chip-scale atomic clock (CSAC). The importance of Doppler, clock quality, receiver sensitivity, and optical navigation is examined through comparison of these results to other instrument configurations. Clock quality (i.e., stability) is the strongest determinant of achievable performance, and the inclusion of GPS Doppler also has a significant effect. Finally, simulation results are compared to two laboratory tests: first a case that includes GPS receiver hardware in the loop, then a case that includes optical navigation and filter flight software in the loop. These agree closely with the simulation results and provide evidence the simulation is accurately modeling the instrument under development.

1. INTRODUCTION

The National Aeronautics and Space Administration (NASA) seeks to establish a sustained presence at the Moon over the next decade through a series of robotic and crewed missions. These efforts will enable a range of science investigations and develop the capabilities and technology required for an eventual crewed journey to Mars. The agency has summarized its intentions in the Moon to Mars Objectives (2022). The lunar south pole is the first destination for crewed missions, a region that presents significant challenges for communications and navigation (Gramling et al., 2022). Orbital geometry (e.g., lunar precession and nutation) and dramatic topography limit direct-to-Earth visibility to less than half of the year, even at the best candidate landing site (Malapert Massif) (Anzalone et al., 2022).

To reduce these constraints on landing site availability and operational safety, NASA will establish a relay constellation to provide communication and position, navigation, and timing (PNT) services at the Moon, with a near-term focus on a service volume within 15 degrees of the south pole. Through NASA's Lunar Communications Relay and Navigation Systems (LCRNS) project, the relays will be owned and operated by commercial service providers, but services must comply with specifications that ensure interoperability (LunaNet, 2022) and meet requirements for functionality and performance (Lunar Relay Services, 2022). For a lunar exploration vehicle to estimate position, velocity, and time (PVT) from a relay radio frequency signal, the relay state must be known with great accuracy and in real time. This paper explores one approach for performing this onboard state estimation and propagation, the LCRNS PNT Instrument (LPI).

To provide services, a lunar relay provider will need to account for all error sources that may contribute to position, velocity and time errors. This would include the relays full PVT estimate, on-board delays, antenna displacements, propagation and representation errors for future times when ephemeris and time estimate products are made available to users and deemed valid. This paper presents errors in the lunar relay PVT and does not intend to represent an all-inclusive error budget for a lunar relay.

2. THE LCRNS PNT INSTRUMENT

The LPI is an instrument being developed at Goddard Space Flight Center (GSFC) to perform onboard, autonomous PVT estimation and state propagation for a spacecraft in lunar orbit, such as a lunar relay. The instrument ingests navigation observables, specifically GPS measurements and optical navigation images, and produces a time-stamped estimate of the relay state (i.e., PVT) as well as a time series of future state estimates. This functionality is achieved through three subsystems: a weak-signal GPS receiver, NavCube3-mini (NC3m); an onboard navigation system, autonomous Navigation, Guidance, and Control (autoNGC); and a clock subsystem, consisting of a frequency reference and pulse-per-second (PPS) source. On LPI, state estimation is performed by autoNGC using the Goddard Enhanced Onboard Navigation System (GEONS), a navigation software library including an Extended Kalman Filter (EKF) developed at GSFC. The core GEONS algorithms have over 20

years of flight heritage, including on the NASA Magnetospheric Multiscale mission (MMS) and Global Precipitation Measurement (GPM) missions (Long et al., 2024). Optical navigation is performed on the autoNGC platform using the core Flight System (cFS) Goddard Image Analysis and Navigation Tool (cGIANT) (Shoemaker et al., 2022). The LPI clock subsystem consists of a 10 MHz frequency reference and pulse-per-second (PPS) source. The clock stability required to deliver PNT services from a lunar relay is still under investigation, but two clocks are considered here: a chip scale atomic clock (CSAC) and a high-end ultra-stable oscillator (USO).

2.1 NavCube3-mini

The NavCube3-mini (NC3m) GNSS receiver is a low size, weight, and power (SWaP) multi-frequency, multi-GNSS receiver designed and built by NASA GSFC as an internal NASA technology development project (see Hassouneh et al. 2023). It derives heritage from the high-altitude GPS receiver Navigator used on the Magnetospheric Multiscale mission (MMS) which launched in 2015 and has been operating for almost a decade in highly elliptic orbits, with apogee distance nearly half that of the distance to the Moon. The NC3m is an evolution of the MMS-Navigator (Winternitz et al., 2017) that specifically targets the lunar regime. NC3m successfully achieved Technology Readiness Level 6 (TRL6) status in late 2022 and continues to be actively updated and enhanced (Hassouneh et al. 2023).

The NC3m receiver consists of a GNSS RF card, processor card, low voltage power converter card (LVPC), backplane card, custom enclosure, and flight software and firmware. Mission-dependent external components include an antenna, front-end electronics, and an optional external oscillator. The GNSS RF card handles down-conversion, filtering, and analog-to-digital conversion for received GNSS signals. The LVPC and backplane provide power services and interconnections between the various cards. The enclosure, built from space-grade hardware, is designed to withstand the stresses of launch and protect against space radiation and electromagnetic interference. Flight software and firmware on the processor card perform baseband signal processing of GNSS signals. FIGURE 1 shows the fully assembled flight-like Engineering Test Unit (ETU) of the NC3m receiver.

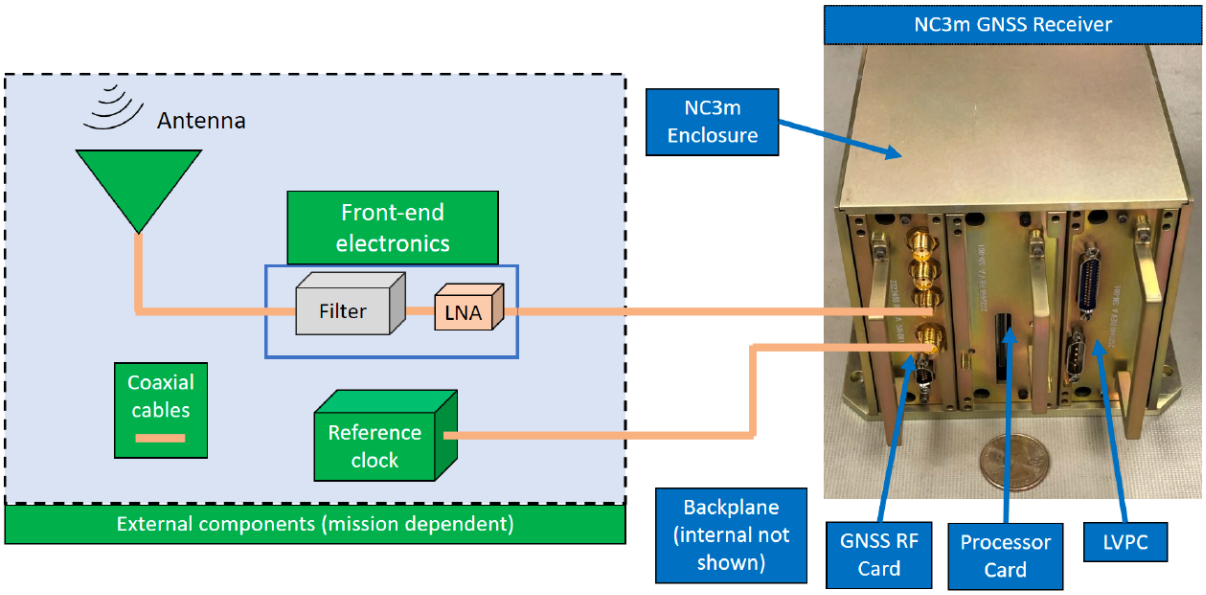

FIGURE 1 NC3m Receiver Hardware

The NC3m system, designed for versatile platform integration, currently utilizes NASA's SpaceCube V3.0 mini processor system architecture (see Brewer et al. 2020). This data processing platform merges the reliability of traditional radiation-hardened components with the cost and performance advantages of commercial parts through a hybrid processing approach. A high-performance commercial FPGA handles data processing, while a separate rad-hard FPGA acts as a supervisor, monitoring radiation upsets and reconfiguring the commercial FPGA as needed. This hybrid approach significantly enhances the cost-to-performance ratio compared to using a single, advanced rad-hard processor and allows for the incorporation of newer parts, as rad-hard versions often lag commercially available ones. The platform's modular design supports a wide range of missions.

The NC3m utilizes a GNSS RF card that offers a flexible, radiation-hardened solution for down-conversion and digitization of GNSS L-band signals. It features two independent RF chains, enabling the processing of signals with different carrier

frequencies, such as the GPS L1 and L2 configuration used in this simulation study. The wide receiver bandwidth also supports signals like GPS L5 and Galileo E5a. The card supports either an on-board or an external reference oscillator and can supply power to an external oscillator. Additionally, it provides a buffered one Pulse Per Second (PPS) signal for timing alignment.

For LPI, NC3m will provide GPS L1, L5 (and potentially Galileo E1/E5a) pseudorange, carrier phase, Doppler and C/N_0 observables to the autoNGC system which fuses them with other observables using GEONS. NC3m also runs an independent copy of GEONS internally for GPS-only measurement processing.

2.2 autoNGC

The autonomous Navigation, Guidance, and Control (autoNGC) subsystem includes onboard flight software and hardware for real-time, autonomous spacecraft NGC (Hur-Diaz, 2024). Instead of missions developing these capabilities from scratch, they can easily infuse the autoNGC flight software and, optionally, hardware, reducing mission cost, schedule, and risk. The flight software is an application suite built on the core Flight System (cFS), which allows customization and insertion of new capabilities, even in flight (Strege, 2016). This plug-n-play software architecture and the low SWaP hardware design enable a wide range of mission types to easily adopt autoNGC.

The autoNGC flight software is a suite of cFS apps as shown in Figure 2 that allow a spacecraft to operate autonomously without support from the ground. The flight software suite includes GEONS, a high-fidelity navigation flight software library that processes sensor measurements to estimate spacecraft position and velocity, onboard clock corrections, and measurement and force modeling parameters (Long et al., 2024). The measurements GEONS can process include GPS observables, one-way and two-way ground station range and Doppler, satellite one-way and two-way crosslink range and Doppler, camera bearing angles, range measurements, accelerometer data, and attitude solutions. Another key library is cGIANT, a version of the advanced image processing tool, GIANT, that uses the cFS architecture (Liounis et al., 2022) GIANT extracts observables from images that can then be processed in GEONS for navigation. The widely available, common cFS software architecture of autoNGC leverages the existing core flight software apps and standardizes integration with the rest of the spacecraft flight software. The cFS software bus provides a standardized plug-and-play interface for the addition of future algorithms and flight software and allows for ready integration into commercial spacecraft that use cFS.

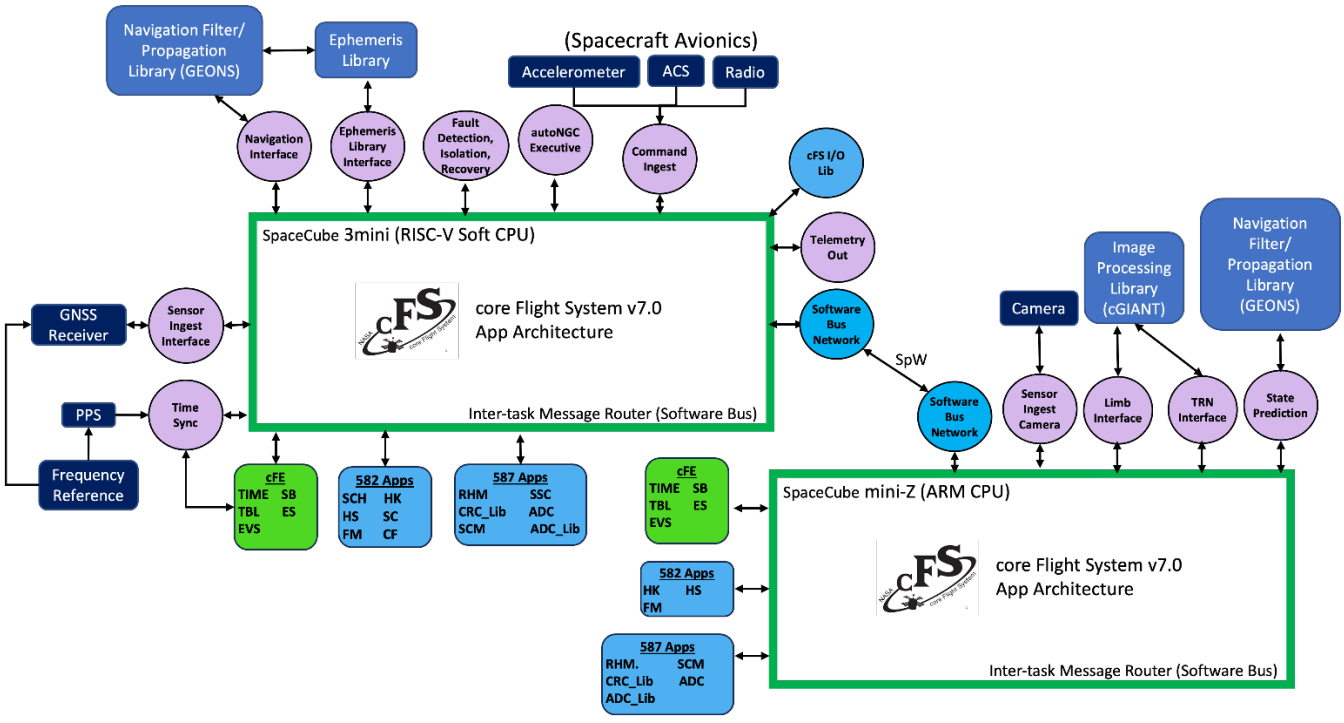

FIGURE 2 Illustration of the autoNGC cFS flight software architecture for LCRNS.

The autoNGC hardware implementation is shown in FIGURE 3. Like NC3m, autoNGC currently utilizes NASA's SpaceCube processor system architecture with a two processor card implementation. The primary, rad-hard processor performs state estimation and essential system functions, while the high-performance secondary card performs state propagation and image processing. The system also includes a low voltage power converter card (LVPC), backplane card, custom enclosure, and custom I/O card.

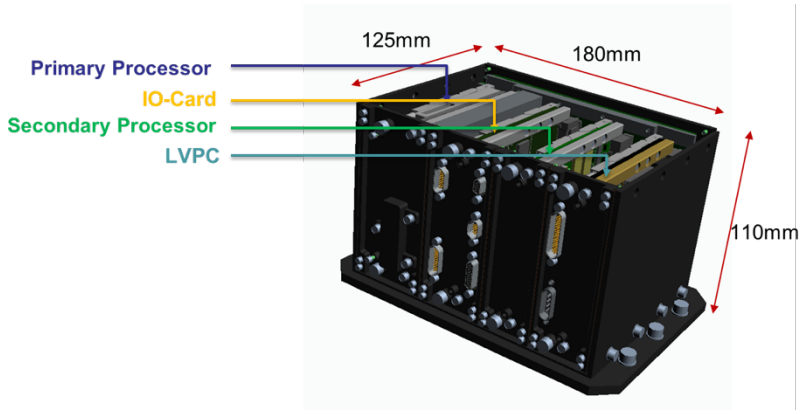

FIGURE 3 autoNGC hardware

3. METHODOLOGY

This analysis examines what onboard, real time navigation performance might be achievable for a satellite in a highly elliptical frozen orbit in a baseline configuration: Measurements of GPS pseudorange and Doppler by a receiver with an acquisition/tracking threshold of 23 dB-Hz and a CSAC. An approximation of a 12-hour frozen orbit is used (Folta et al., 2006) with an apolune over the lunar south pole and an orbital plane oriented such that GPS is not occulted by the Moon for the four-day duration of the simulation. The orbit used is not strictly frozen (orbital parameters evolve at timescales longer than the simulation period) and the actual period is 13.19 hours. The orbit is shown in FIGURE 4 and key parameters are given in

TABLE ***1***; Cartesian coordinates are in terms of ICRF (close to MJ2000Eq) centered at the lunar center of mass. The inclination of the orbit is referenced to the Moon orbital plane, i.e., the plane of the Earth's apparent motion relative to the Moon, as described in Folta et al., 2006. A frozen orbit's spacecraft orbital plane precesses about the Moon's orbital plane z-axis.

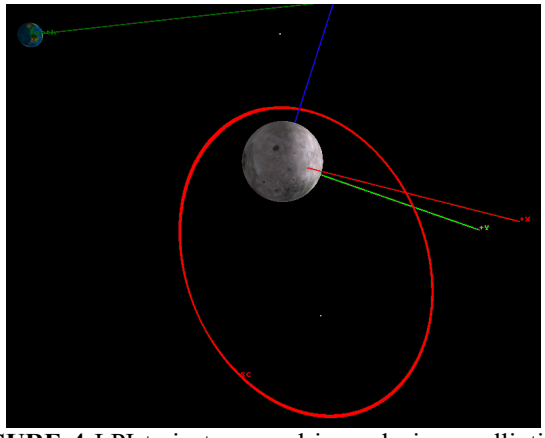

FIGURE 4 LPI trajectory used in analysis: an elliptical lunar orbit viewed in the International Celestial Reference Frame (ICRF) centered at the Moon (the distant Earth is visible in the top left of the figure)

TABLE 1 Orbital parameters

Epoch	May 27, 2024, 12:16:34 UTC
Initial semi-major axis	6541.4 km
Initial inclination relative to Moon orbital plane	56.2°
Eccentricity	0.6
Initial true anomaly	0°
Initial position [km] (ICRF centered at the lunar center of mass)	-1385.3935, -819.2177, 2062.9963
Initial velocity [km/s] (ICRF centered at the lunar center of mass)	2062.9963, -1.5017, -0.8044

The importance of GPS Doppler, clock quality, receiver sensitivity, and optical navigation is examined through comparison of baseline results to other instrument configurations. Each case is run for four days to allow the filter to reach a steady state, with state estimates performed by the EKF every ten seconds. One hundred Monte Carlo runs varying all stochastic parameters are performed for each case to generate performance statistics. For the simulation runs, the LPI is modeled using the GEONS Ground MATLAB Simulation (GGMS), a collection of MATLAB scripts that calls the GEONS flight software library to simulate and process measurements and produce estimated states and covariance updates. The filter setup and measurement models are described below.

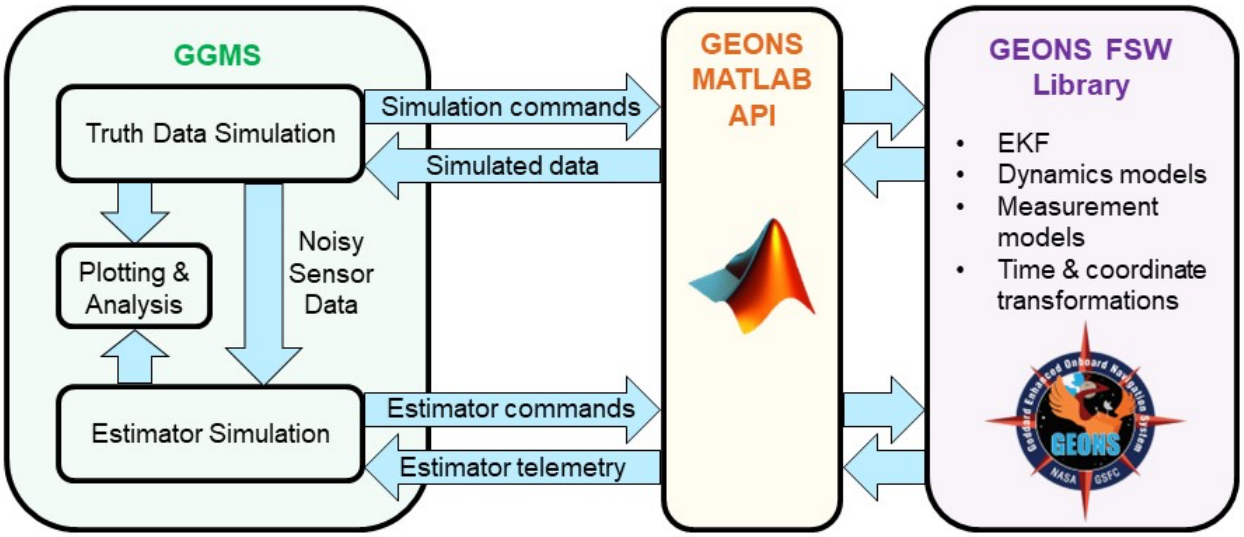

FIGURE 5 Block diagram conceptual illustration of how GGMS uses GEONS to simulate and process measurement data.

3.1 Filter Setup

GEONS uses a factorized EKF to estimate the spacecraft state and other dynamical model parameters in real time from onboard sensor measurements. Filter and simulation parameters are shown in TABLE 2. In this study, the estimated state vector includes spacecraft position, velocity, and solar radiation pressure (SRP) coefficient correction, as well as clock bias, drift, and drift rate. Covariance propagation in the EKF includes velocity and clock process noise models that are adjusted to provide a predicted covariance that is consistent with the estimation errors. The velocity process noise model includes higher dynamics

modeling errors at perilune versus apolune. The clock process noise model is consistent with the Hadamard variances of the clock used in the simulation.

TABLE 2 Filter / simulation parameters

Parameter	Value
Dry mass	273.85 kg
SRP model	Spherical
SRP area	4.767 m^2
Coefficient of Reflectance	1.2
Solar flux	1367 W/m^2
Reference distance for solar flux	Sun-Earth average distance
Lunar gravitational model	GRGM 900C
Lunar gravitational degree	100 (truth), 18 (filter)
Lunar gravitational order	100 (truth), 18 (filter)
Propagator	RungeKutta4
Orientation of Moon body frame	DE421
Planetary ephemeris	DE421
Earth Orientation Parameters	IERS Bulletin A from 5/30/24 (truth and filter)

3.2 Measurement Models

Onboard measurements include GPS pseudorange, GPS Doppler, and optical navigation, specifically Terrain Relative Navigation (TRN).

3.2.1 Global Positioning System

The GPS constellation state is simulated using a broadcast ephemeris from January 1-9, 2022, adjusted to the simulation epoch. The transmit properties of the satellites are modeled using per-satellite transmit gain as a function of off-boresight azimuth and elevation from a combination of data from the GPS Antenna Characterization Experiment (Donaldson et al., 2020) and publicly released GPS transmit patterns (U.S. Coast Guard, 2024). Transmit power for each satellite is calibrated using flight data from the Magnetospheric Multiscale (MMS) mission, a formation of four spacecraft using GPS for navigation halfway to the Moon (i.e., transmit power inferred from received signal strength and gain pattern data, see Winternitz et al., 2019 for details). On the user spacecraft, a high gain parabolic antenna is assumed to maintain Earth pointing throughout the simulation. Peak gain is approximately 16 dBi at the antenna boresight, modeling a roughly half-meter antenna that covers the constellation at lunar distance without overly constraining pointing.

Error between the simulated Earth Orientation Parameters (EOPs) and the predicted EOP's is not modeled in these simulations. LPI will use EOPs from GPS CNAV Message Type-32, so this unmodeled effect is expected to be small. Although the relativistic effects of Earth point mass gravity on clock frequencies are included, other relativistic effects on GPS signals are not included in this analysis.

GPS pseudorange and carrier phase are computed at the true UTC receiver time using the geometric difference between the true receiver location at the time of reception and the true GPS satellite location at the time of transmission plus a model of GPS satellite ephemeris errors, receiver time bias, GPS-system biases, ionospheric errors, GPS satellite time error, and random measurement noise. Pseudorange and carrier phase noise standard deviations are computed using additive random error models based on GPS thermal noise theory; noise is a function of carrier-to-noise spectral density (C/N_0) of the received signal and tracking loop bandwidth parameters (e.g., see Kaplan et al., 2017). GPS Doppler is computed by differencing two carrier phase observables at two different times and dividing the result by the time difference T (10 seconds in the simulations below). This gives an average Doppler observable over the differencing interval with the high precision of carrier phase observables and units of cycles/s or Hertz. The standard-deviation of the Doppler measurement is $\sqrt{2}/T$ times the phase noise of the individual observables, with a contribution from the clock noise that depends on the T-second stability measure. To clearly indicate that this is a high precision, carrier phase-derived Doppler, this measurement type is referred to as time-differenced carrier phase Doppler (TDCP-Doppler) below.

3.2.2 Terrain Relative Navigation

TRN involves the correlation of onboard navigation maps, rendered on-board using the current state estimate and digital terrain models (DTMs) of the surface, with real time images from an onboard navigation camera. The small sections of the target DTM used for TRN are called "maplets," with a "landmark" representing the origin of the maplet (Shoemaker et al., 2022). The range and bearing (i.e., azimuth and elevation) of the landmark relative to the spacecraft can be estimated from this correlation. In the simulation cases here, measurements are simulated as unitless line-of-sight bearing measurements of the form $\left(\frac{x}{z}, \frac{y}{z}\right)$ in the camera frame defined with +x parallel to the rows of the detector, +y parallel to the columns of the detector, and +z out of the camera into the world (Section 5.8.2.3 in Long et al., 2024).

Bearing measurements are generated to five surface landmarks per image, one image per minute. Zero mean Gaussian noise is applied to the simulated measurements with a very conservative noise of 2-pixels standard deviation for a 40-degree field of view, 4 mega pixel camera. The landmarks are assumed to be uniformly distributed on the surface of the Moon. For each image, only visible landmarks are considered (checking that the landmark is within the camera field of view, is not occluded from the camera, and is illuminated by the sun). From the list of visible landmarks, 5 are selected to process to represent the limits of flight hardware.

3.3 Clock Model

Two clocks are considered here: a CSAC and USO. The properties of each are shown in TABLE 3.

TABLE 3 Clock models

		Clock State Time Variance q-values		
Clock Model	**10 sec Allan Dev**	**q1**	**q2**	**q3**
USO	3.30e-12	1.1e-22	1.4e-26	5.9e-75
CSAC	7.61e-12	5.8e-22	1.5e-29	1e-45

Each Monte Carlo simulation models a separate truth clock. Truth clock states are used to simulate the GPS observables that are then processed by the EKF. General and Special Relativistic effects are not included in the truth clock state updates.

At each time step the clocks are modeled with three states: clock bias, clock drift, and clock drift rate. Clock bias is the current time difference between the modeled LPI Time and UTC multiplied by the speed of light to change the units to meters. Clock drift and drift rate are the first and second time derivatives of the clock bias with respect to UTC. The clock state time variance q-values are the one second expected time variance of the associated clock states. For example, if the USO clock bias at time step 0 is 0 meters, the clock drift is 0 m/s, the drift rate is 0 m/s^2, and the q-values are given as the "USO model" in TABLE 3. After 10 seconds, the standard deviation for the expected clock bias would be $\sqrt{1.1e^{-22} \times 10} \times c = 1.0e^{-3}$ m, the expected clock drift standard deviation would be $\sqrt{1.4e^{-26} \times 10} \times c = 1.1e^{-4}$ m/s, and the expected clock drift rate standard deviation would be $\sqrt{5.9e^{-75} \times 10} \times c = 7e^{-29}$ m/s^2. A better performing clock improves the GPS measurement accuracy and results in a more stable clock bias that is easier for the EKF to estimate. This is particularly important in the case of 1-way observables like GPS, as clock errors can be difficult to distinguish from range errors.

Each Monte Carlo simulated clock model is initialized with randomly sampled clock states. The clock is modeled by a second order random walk process, with process noise determined by the q-values and time step interval (Long 2024). Reference (Hutsell, 1995) provides additional detail and includes an approach for relating Hadamard Variance or Allan Deviation values to q-values for a given clock.

4. SIMULATION RESULTS

Monte Carlo analysis is used to evaluate what onboard, real time navigation performance might be achievable for the baseline configuration of LPI. This baseline case consists of GPS pseudorange and TDCP-Doppler with a 23 dB-Hz acquisition and tracking threshold and a CSAC in a highly elliptical lunar orbit. The baseline case is compared to alternate cases to examine the relative importance of GPS Doppler, clock quality, receiver sensitivity, and optical navigation.

FIGURE 6 shows the root-sum-square (RSS) position errors and RSS velocity errors for the baseline case. The RSS error is calculated for each Monte Carlo run as the magnitude of the position or velocity error vector at each time step. Errors for each of the 100 Monte Carlo cases are plotted in grey and the formal error is plotted in green over the four days of the simulation.

The formal error is calculated as three times the square root of the diagonals of the average of the 100 Monte Carlo covariances; this approximates a 99.7-percentile of the RSS errors according to the formal filter covariance and is labeled as "3σ cov" in the following figures.

After the initial convergence of the filter, errors oscillate throughout each orbit; position errors are highest at apolune, and velocity errors are highest at perilune. This baseline case is repeated on the left side of the four subsequent figures for comparison to the alternate configurations. In all cases the estimation errors are roughly consistent with the formal error metric calculated from the filter covariance.

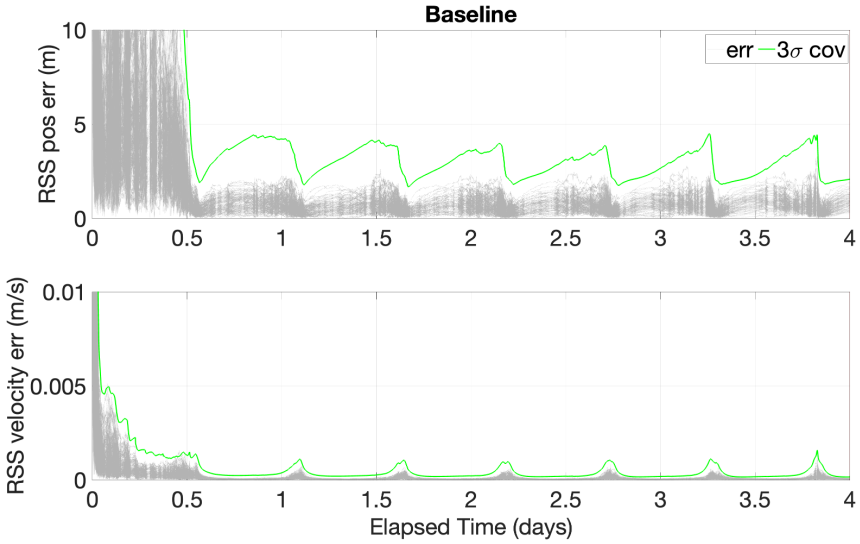

FIGURE 6 Position and velocity errors for the baseline case (GPS pseudorange and TDCP-Doppler, 23 dB-Hz acquisition/tracking threshold, and a CSAC)

In FIGURE 7, the baseline case is compared to a case where the acquisition/tracking threshold of the GPS receiver is 27 dB-Hz. This change in receiver sensitivity has little effect. The number of GPS signals above 23 dB-Hz in this lunar orbit is only slightly greater than the number above 27 dB-Hz and the resulting position and velocity errors are largely unchanged. In FIGURE 8, the baseline case is compared to a case where only GPS pseudorange is used (i.e., no TDCP-Doppler). This significantly increases the convergence time and steady state errors for both position and velocity; note that the vertical axis of both the baseline and pseudorange only plots have been increased relative to the other figures. FIGURE 9 compares the baseline case to a case using a USO rather than a CSAC. The use of a USO also increases the steady state errors, though not as much as when TDCP-Doppler is removed. Finally, TRN is added in FIGURE 10, but for the orbit under study this has little effect.

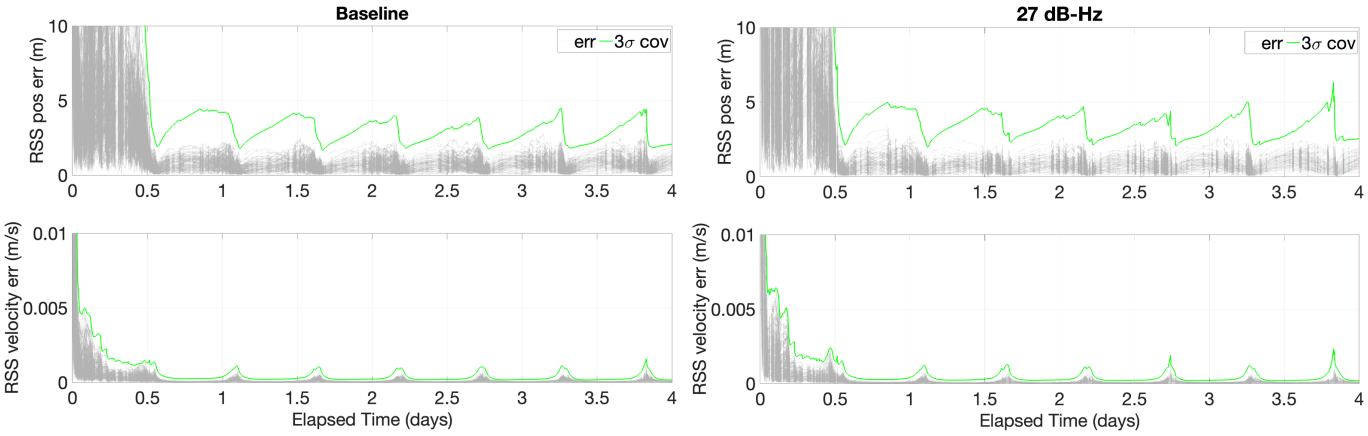

FIGURE 7 Comparison of baseline case (left) and case with a less sensitive GPS receiver (right), i.e., acquisition/tracking threshold degraded from 23 dB-Hz to 27 dB-Hz

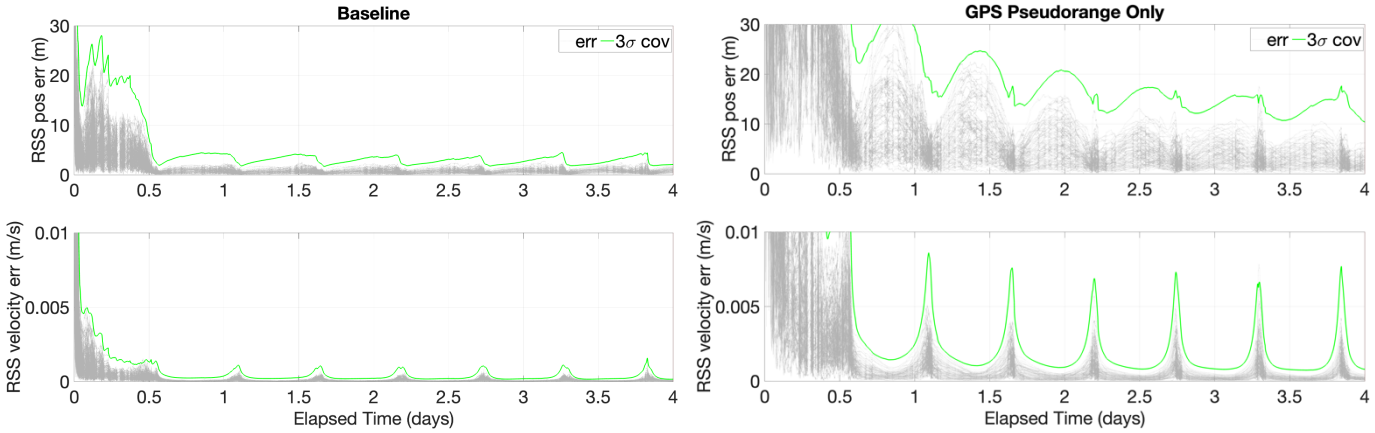

FIGURE 8 Comparison of baseline case (left) and a case with only GPS pseudorange (i.e., no TDCP-Doppler)

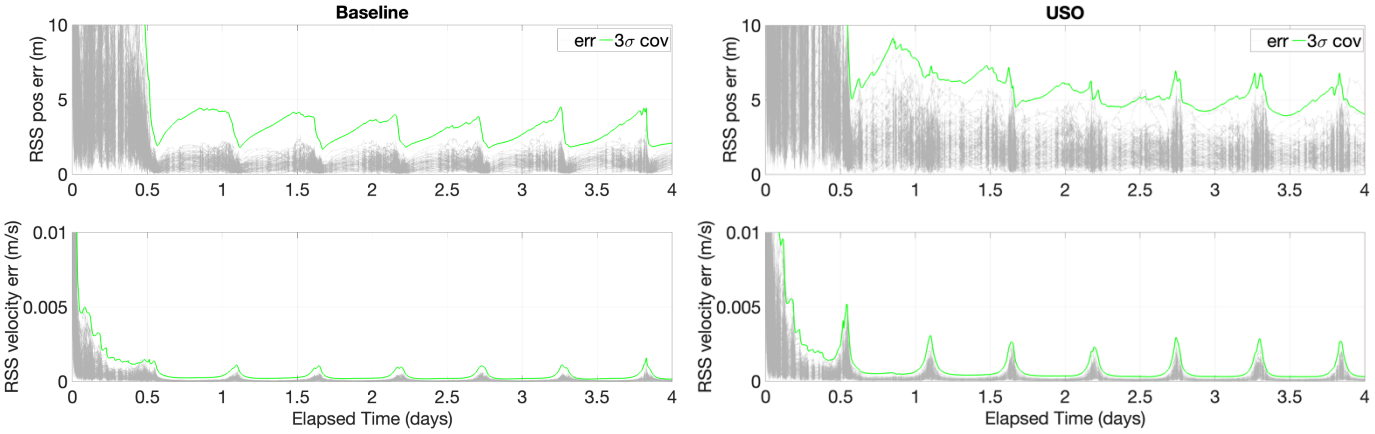

FIGURE 9 Comparison of baseline case (left) and case with a USO instead of the CSAC

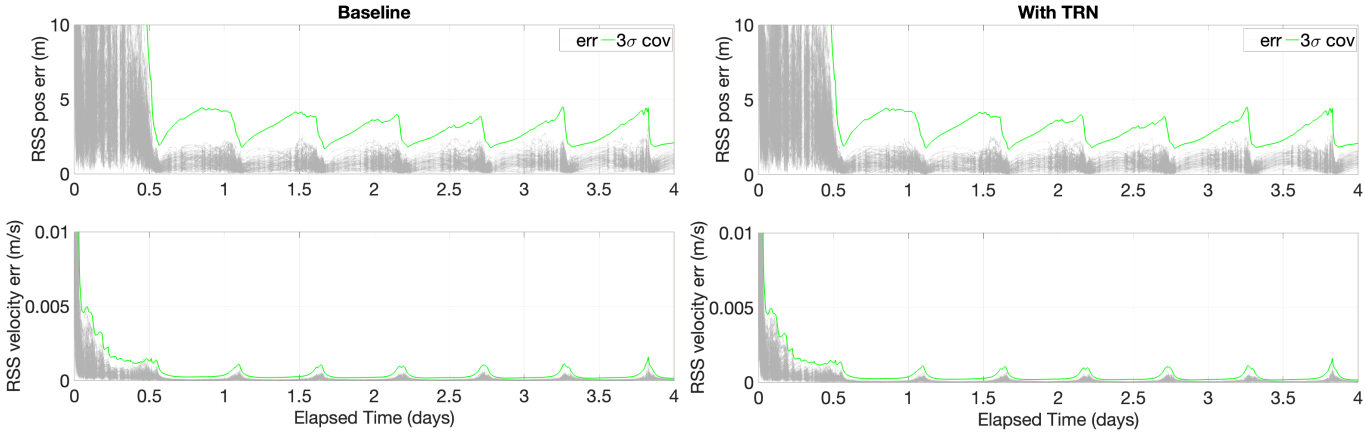

FIGURE 10 Comparison of baseline case (left) and case with TRN measurements added (right)

4.1 Summary of Simulation Results

TABLE 4 compares the steady state errors from the Monte Carlo simulation of all cases discussed above. These statistics are computed by considering just the timespan from 45 minutes after perilune in the 7th orbit to 45 minutes before the next perilune; this focuses on the portion of the orbit in view of the lunar south pole region. These times correspond to 3.326 days to 3.813 days from the start of the simulation. This segment is shown in FIGURE 11.

The 95th percentile of all RSS values across the one hundred Monte Carlo cases is reported in TABLE 4. The same calculation is performed for velocity errors. The 95th percentile of the clock bias and drift magnitudes is also reported over the same time span. These statistics corroborate the conclusions drawn from the above figures: an increase in the receiver acquisition/tracking threshold to 27 dB-Hz does not significantly affect the errors and nor does the addition of TRN measurements. Changing from a CSAC to a USO does increase position and velocity errors, but not as much as removing GPS TDCP-Doppler measurements (except in the case of clock drift errors, which are lower in the CSAC/TDCP-Doppler case).

TABLE 4 Summary of simulation steady state errors

Results Figure	Measurements			Analysis Modeling Parameters		100-case Monte Carlo statistics – 7th orbit in view of lunar south pole				
	GPS pseudo-range	GPS TDCP-Doppler	TRN	GPS acq/trk threshold [dB-Hz]	Clock model	RSS position error [m] 95th percentile	Clock bias magnitude error [m] 95th percentile	RSS velocity error [mm/s] 95th percentile	Clock drift magnitude error [mm/s] 95th percentile	Clock drift rate magnitude error [$\mu m/s^2$] 95th percentile
4	X	X		23	CSAC	1.53	1.63	0.133	0.090	0.0038
5	X	X		27	CSAC	1.71	1.82	0.146	0.103	0.0038
6	X			23	CSAC	6.39	2.91	0.624	0.285	0.0040
7	X	X		23	USO	2.60	2.00	0.297	0.475	0.1397
8	X	X	X	23	CSAC	1.54	1.59	0.138	0.090	0.0043

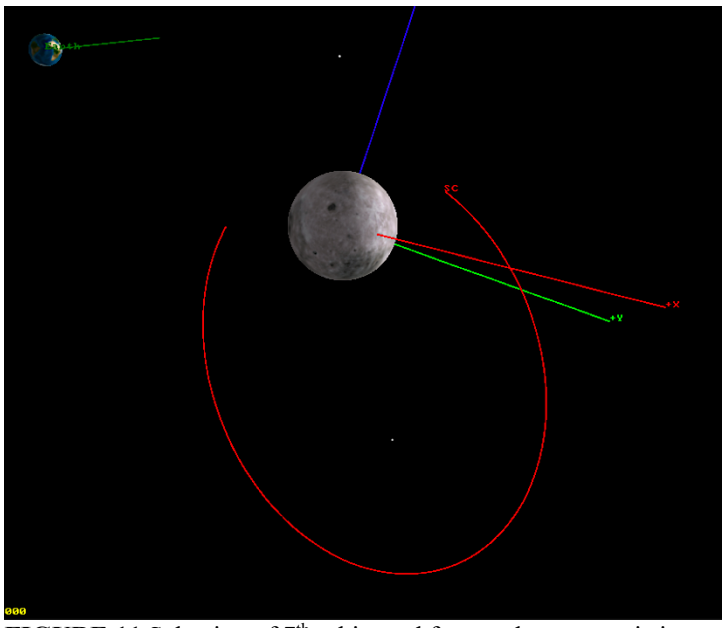

FIGURE 11 Selection of 7th orbit used for steady state statistics

5. COMPARISON TO LAB RESULTS

The Monte Carlo analysis discussed above relies on simulated GPS observables provided by a model of the NC3m GNSS receiver and TRN observables provided by a model of GIANT image processing and optical navigation software. To demonstrate the validity of these models, a high-fidelity hardware-in-the-loop (HWIL) simulation is developed and run on the NC3m receiver, with signals provided by a GPS constellation simulator, and a software-in-the-loop (SIL) simulation is developed and run on the autoNGC flight software using synthetic images of the lunar surface.

5.1 NC3m Hardware in the Loop

For the HWIL simulation, GPS measurements are provided to the NC3m by a high-performance Spirent 9000 series GNSS simulator (Spirent 9000 product webpage 2024) locked to a laboratory Cesium frequency reference. The simulation follows the same 4-day LPI trajectory used in the GGMS Monte Carlos and uses the same transmit and receive antenna patterns. Special care is taken to calibrate the HWIL and GGMS-simulated GPS power levels using MMS flight data to produce realistic in-orbit signal levels. Adjustments are made to account for in-orbit versus laboratory noise levels, etc. A 3dB link margin is included, as in the GGMS sims.

There are some known modelling differences between the GGMS and HWIL simulation that can result in minor differences in the results. In the HWIL simulation, the GPS constellation orbits are specified using the first entry of the broadcast ephemeris used in the GGMS simulation (TABLE 2) and then propagated using the GNSS simulator to avoid discontinuities at transitions between ephemerides. This results in increasing differences in the GPS constellation between the GGMS and HWIL simulations over time. The HWIL sim uses a less accurate model for GPS transmitter yaw than GGMS, so signals received from GPS sidelobes are not identical. These sidelobe signals, which have significant azimuthal gain variation, do not exactly match those in the GGMS sim. The levels are qualitatively consistent, however, as shown in FIGURE 12. Differences also arise from the inherent randomness in the signal acquisition process as well as random variations in the clock and measurement processes of the two simulations.

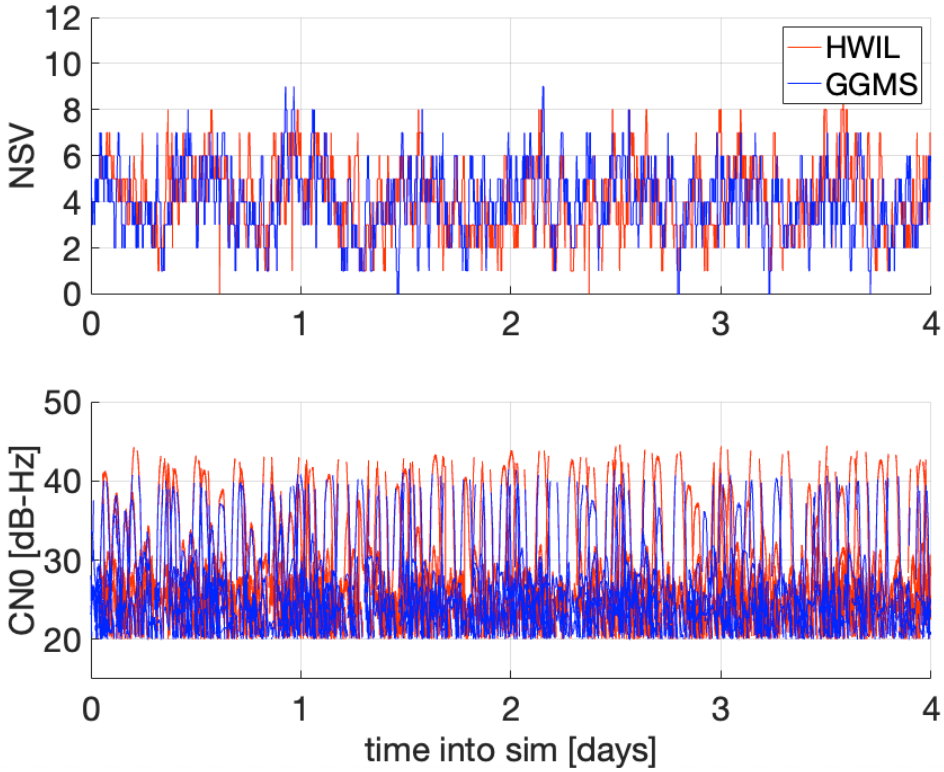

FIGURE 12 NC3m HWIL (red) and corresponding GGMS sim (blue) number of visible signals (top) and C/N_0 (bottom)

The HWIL simulation is executed on a development version of the NC3m receiver (with the same performance as the TRL6 unit) using a high performance USO as the primary frequency reference. This USO has similar stability and phase noise as the USO modeled in the GGMS simulation. For this analysis, the receiver's internal GEONS filter is configured to process L1 C/A pseudorange only and is tuned in a manner consistent with the GEONS filter in the GGMS simulations described above. Truth data is logged from both the HWIL and GGMS simulations and used to evaluate performance of the receivers over the full trajectory. In FIGURE 13, results from the HWIL simulation are compared to a single case GGMS simulation set up as described in Section 3 but with a reduced acquisition/tracking threshold of 20 dB-Hz, rather than 23 dB-Hz, and minor tuning adjustments to match the known hardware settings and behavior as close as possible. (Note: While similar GEONS results were obtained during the HWIL run, the results shown in FIGURE 13 were obtained by reprocessing the receiver observables and decoded broadcast ephemerides collected during the HWIL in GEONS offline in order to correct a minor filter configuration issue.)

Overall, the GGMS and HWIL simulations match closely. The number of signal tracked and C/N_0 levels, shown in FIGURE 12, are qualitatively very similar. The main lobe signals match well at the beginning of the sim when the constellations are closely aligned. Apart from this, the main lobe and sidelobes, seen as the denser grouping generally below 30 dB-Hz, match well on average. In the HWIL simulation, signals are tracked closer to the limb of the Earth than in the GGMS simulation and reach high peak C/N0 levels, but these signals may have significant ionosphere-induced delays and may be omitted from processing in the HWIL GEONS filter. FIGURE 13 shows a comparison of the GEONS filter position and velocity RSS estimation and formal errors. Again, the results are very similar between the two simulations, and well within the expected variation due to the differences described above.

These results indicate that the NC3m receiver performance is consistent with the receiver model used in the GGMS simulations. Given that the GGMS simulations have been carefully calibrated against real-world on-orbit data from the high-altitude MMS mission, these results provide evidence that the simulations in this paper provide a realistic prediction of the performance of the LPI's GPS-based navigation.

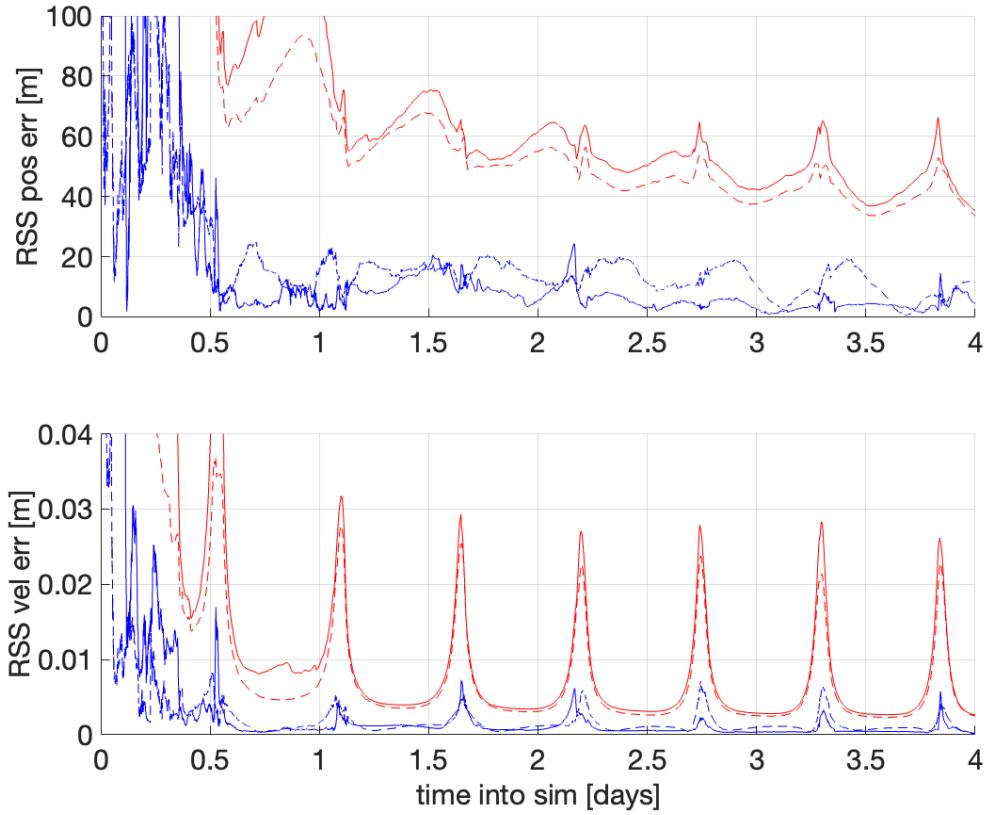

FIGURE 13 NC3m HWIL (solid) and identical GGMS run (dashed); formal errors (obtained from the filter covariance) are in red, estimation errors are in blue

5.2 autoNGC Software in the Loop

A high-level block diagram description of the SIL architecture is provided in FIGURE 14. The simulation software generates data, command, and telemetry packets consistent with what is expected to be received by the flight software in orbit. This data is sent to and processed by the autoNGC flight software, which is described in Section 2.2. Telemetry from the flight software is sent to the COSMOS ground software (OpenC3, Inc., 2023). GGMS is used to generate configuration files for the simulation and flight software for the considered scenario. For this paper, the SIL testing was configured to be consistent with the GGMS Monte Carlo simulations above unless otherwise specified.

The simulation software is composed of a general-purpose 6-degree-of-freedom simulation tool called 42 (Stoneking, 2018), a set of Python and C++ code referred to as *sim_all*, an instance of GEONS in *sim_all*, and image generation software built on GIANT. The reference truth trajectory is generated in 42, which is then read into *sim_all*. At each time step (~10 s), *sim_all* commands GEONS to propagate the simulated truth clock error states (e.g., onboard clock offset and drift) to the current time, commands the 42 true spacecraft state into GEONS, and then commands GEONS to simulate GPS measurement data. When propagating the truth clock error states, GEONS randomly samples and adds process noise to the clock error states consistent with the clock parameters specified in this paper. The simulated clock error states are used in the simulation of the GPS observables. The instance of GEONS in the simulation software is run separately from the instance of GEONS running in autoNGC. In *sim_all*, the simulated GPS data is formatted as NC3m packets containing GPS observables (pseudorange, Doppler, carrier phase, C/N_0) and broadcast ephemeris data, which are then sent to the flight software.

Additionally, on the requested imaging cadence (60 seconds for this paper), *sim_all* sends the truth state information to the camera simulator (*sim_camera*) over user datagram protocol (UDP), which renders a simulated image of the moon using ray tracing and sends a capture image command to the flight software. The flight software then requests a new image from *sim_camera* (which has been configured to mimic talking to actual camera hardware) again through UDP. *Sim_camera* packages the image and then returns it to the flight software.

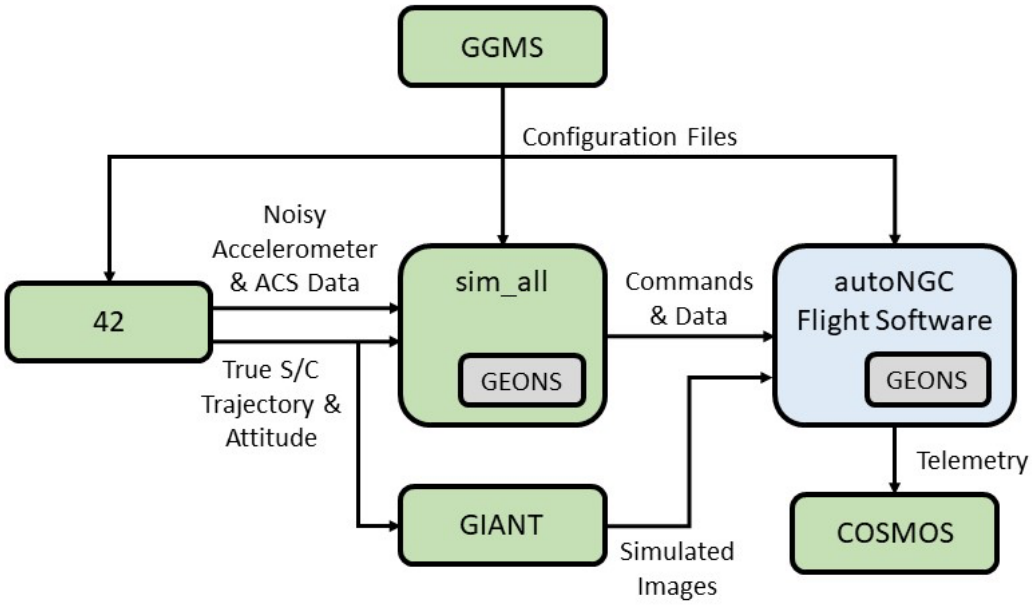

FIGURE 14 Block diagram illustration of the autoNGC SIL architecture. Blue indicates flight software, green is ground and simulation software, and gray is GEONS, which is run separately in both the simulation and flight software.

The autoNGC flight software is illustrated in FIGURE 2. Most commands/data sent to the flight software are ingested by the *command_ingest* app, which publishes them onto the flight software bus. The *ngc_geons* app subscribes to all messages on the software bus that are needed for the navigation filter (e.g., GPS data) and commands them into GEONS. The simulated lunar images are requested and received by the sensor ingest camera app, *si_camera*, and then processed in the TRN app (*ngc_trn*). This app uses the cGIANT library to extract bearing measurements to individual landmarks. To extract these measurements, cGIANT uses templates of the lunar topography stored onboard to render predicted maps using ray tracing and then match them to the simulated image using normalized cross correlation. This simulation includes full image processing and TRN; therefore, additional noise is not added to the extracted bearing measurements. These bearing measurements are published on the software bus, ingested by *ngc_geons*, and then commanded into GEONS. Telemetry from the autoNGC flight software is output to the COSMOS ground software. This telemetry includes the estimated state vector and its associated error covariance, the onboard clock time and associated corrected time based on the clock offset estimated in GEONS.

Results for two SIL scenarios and corresponding GGMS Monte Carlo results are shown in FIGURE 15. On the left, the only measurement type was GPS pseudorange, while on the right TRN was added. These two scenarios were otherwise consistent with the previously described baseline GGMS Monte Carlo scenario except that the SIL scenarios used a USO clock model (note that the GGMS case in TABLE 4 with the USO included TDCP-Doppler, so this configuration was different). The SIL results are consistent with the corresponding GGMS Monte Carlo simulations. Furthermore, TRN measurement residuals were similar between the SIL test and corresponding GGMS runs, indicating that the TRN modeling in GGMS is representative of the real image processing in the SIL. For this scenario, TRN did not significantly impact the filter formal error covariance, but it did slightly reduce the size of the estimation errors during convergence. TRN performance can easily be improved with a detector with a smaller instantaneous field of view (IFOV) and by tracking more features per image, and additionally may perform better in other orbital configurations. TRN is expected to be more beneficial when there are GPS measurement outages or a lower altitude orbit is used.

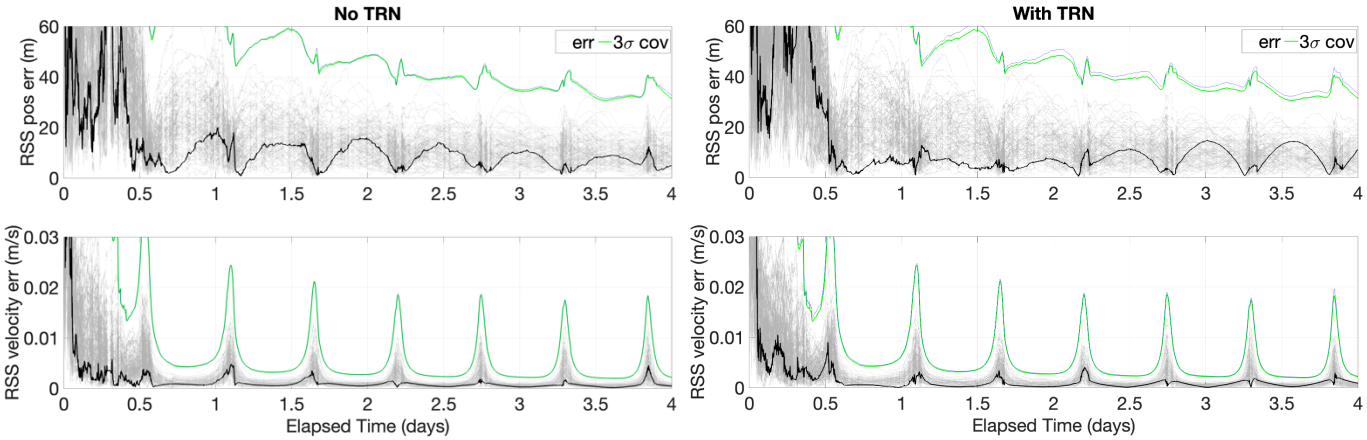

FIGURE 15 SIL single run errors (black) and formal errors (blue) overlaid on 100 GGMS Monte Carlos (gray) and formal error (green) with only GPS pseudorange (left) and with the addition of TRN (right)

6. CONCLUSIONS

This paper introduces the LCRNS PNT Instrument (LPI), an instrument that can employ a variety of measurements, such as GPS pseudorange, GPS time-differenced carrier phase Doppler (TDCP-Doppler), and terrain relative navigation (TRN), to estimate the host spacecraft state onboard and in real time. This approach to determining position, velocity, and time (PVT) enables a level of spacecraft autonomy not possible in a traditional ground-based tracking approach. In particular, onboard PVT estimation enables the accuracy of real time state knowledge, short-turnaround ephemeris updates, and time transfer required by the LCRNS lunar relays for delivery of PNT services to lunar users.

A Monte Carlo analysis is conducted to examine the sensitivity of different parameters: measurement combinations (e.g., with and without GPS TDCP-Doppler, with and without TRN), GPS receiver sensitivity, and clock performance. A baseline configuration consisting of GPS pseudorange and time differenced carrier phase Doppler with a 23 dB-Hz acquisition/tracking threshold and a CSAC is shown to achieve position knowledge on the order of meters and velocity knowledge better than a millimeter per second on the last orbit of a four-day simulation while in view of the lunar south pole. Degradation of receiver acquisition/tracking threshold to 27 dB-Hz does not significantly increase the errors for scenario studied here. The addition of TRN measurements does not reduce steady state errors in the analyzed scenario, though it provides robustness and measurement redundancy benefit in this scenario and is expected to greatly benefit landers and potentially also scenarios in low lunar orbit. Changing from a CSAC to a USO does degrade navigation performance, but not as much as removing GPS TDCP-Doppler measurements. Hardware in the loop (HWIL) and software in the loop (SIL) runs build confidence in the Monte Carlo results.

The PVT estimation achieved in these simulations is excellent. There is no exact comparison but consider the following examples: the Lunar Reconnaissance Orbiter (LRO) meets its 50-meter position requirement through daily 8- to 10-hour ground station tracking passes, an onboard altimeter, and extensive post-processing over several days of data (Mazarico et al., 2017). Previous analysis of the Gateway orbit (a near-rectilinear halo orbit) showed maximum steady-state errors between 100 and 160 meters for DSN-based navigation and 20 to 50 meters for GPS-based navigation (Ashman et al., 2021). The LCRNS Services Requirements Document (SRD) cites 100-meter position knowledge as a representative user need in low lunar orbit (Lunar Relay Services, 2022). The Monte Carlo analysis presented here suggests that LPI could be a critical enabling technology for onboard, real-time navigation of spacecraft exploring the Moon, or spacecraft providing PNT services via lunar relays to the growing lunar ecosystem.

ACKNOWLEDGMENTS

The work presented in this paper was funded by NASA's Lunar Communications Relay and Navigation Services (LCRNS) project.

REFERENCES

Anzalone, E., Gramling, C. (2022). Orbital – Surface Lunar Architecture for PNT (O-SLAP). NASA.

Ashman, B. W., Schlenker, L. G., Parker, J. J., Bauer, F. H., Winternitz, L. B., Long, A. C., ... & Hassouneh, M. A. (2021, May). Applications and Benefits of GNSS for Lunar Exploration. In *16th International Conference on Space Operations*.

Brewer, C., Franconi, N., Ripley, R., Geist, A., Wise, T., Sabogal, S., Crum, G., Heyward, S., & Wilson, C. (2020). NASA SpaceCube Intelligent Multi-Purpose System for Enabling Remote Sensing, Communication, and Navigation in Mission Architectures. *Proceedings of Small Satellite Conference 2020, Virtual*.

Donaldson, J. E., Parker, J. J., Moreau, M. C., Highsmith, D. E., & Martzen, P. D. (2020). Characterization of on-orbit GPS transmit antenna patterns for space users. *NAVIGATION: Journal of the Institute of Navigation*, *67*(2), 411-438.

Folta, D., & Quinn, D. (2006, August). Lunar frozen orbits. In *AIAA/AAS Astrodynamics Specialist Conference and Exhibit* (p. 6749).

Gramling, C., Crenshaw, J., & Mann, L. (2022). Interoperable Services to Mitigate Lunar Position, Navigation, and Timing Challenges. In *73rd International Astronautical Congress*.

Hassouneh, M. A., Midkiff, D., Winternitz, L. B., Price, S. R., Thomas, L., Hatke, D., Lee, T., Bamford W., & Mitchell, J. W. (2023). NavCube3-mini Lunar GNSS Receiver. *Proceedings of the Institute of Navigation GNSS+ 2023, Denver, CO*.

Hur-Diaz, S., Azimi, B., Romeo, M., Liounis, A., Stacey, N., Pritchett, R., Crum, G., Semper,S. (2024). Autonomous Navigation, Guidance, and Control Software in a Low SWaP Box. *NASA Technical Reports Server (NTRS)*. https://ntrs.nasa.gov/citations/20240008867

Hutsell, S. T. (1995, December). Relating the Hadamard variance to MCS Kalman filter clock estimation. In *Proceedings of the 27th Annual Precise Time and Time Interval Systems and Applications Meeting* (pp. 291-302).

Kaplan, E., & Hegarty, C. (Eds.). (2017). *Understanding GPS/GNSS: principles and applications*. Artech house.

Liounis, A. J., Gnam, C., Swenson, J., Getzandanner, K., Small, J., & Lyzhoft, J. (2022). The Goddard Image Analysis and Navigation Tool (Version 1.0.3) [Computer software]. https://github.com/nasa/giant

Long, A., Gaylor, D., & Stacey, N. (2024). Goddard Enhanced Onboard Navigation System (GEONS) Mathematical Specifications Release 3.0. *NASA Technical Reports Server (NTRS)*. https://ntrs.nasa.gov/citations/20240004259

Lunar Relay Services Requirements Document (2022). https://esc.gsfc.nasa.gov/static-files/ESC-LCRNS-REQ-0090%20Rev_B%2012-05-2022%20DCN001.pdf

LunaNet Interoperability Specification v4 (2022). https://www3.nasa.gov/sites/default/files/atoms/files/lunanet_interoperability_specification_version_4.pdf

Mazarico, E., Rowlands, D. D., Neumann, G. A., Smith, D. E., Torrence, M. H., Lemoine, F. G., & Zuber, M. T. (2012). Orbit determination of the lunar reconnaissance orbiter. *Journal of Geodesy*, *86*, 193-207.

Moon to Mars Objectives (2022). https://www.nasa.gov/wp-content/uploads/2022/09/m2m-objectives-exec-summary.pdf

OpenC3, Inc. (2023). The Software for Integration, Test, and Operations. https://openc3.com/

Spirent 9000 product webpage. (2024) https://www.spirent.com/products/gnss-simulator-gss9000.

Shoemaker, M. A., Hur-Diaz, S., Liounis, A., Van Eepoel, J., Romeo, M., Wu, V., Dangelo, S., Hatten, N., Schlenker, L., Hughes, S., Price, S., & Winternitz, L. (2022). Terrain relative navigation in a lunar landing scenario using autongc. In *AIAA SciTech 2022 Forum* (p. 0744).

Strege, S. (2016). CFS A Paradigm Shift in Flight Software Development. https://cfs.gsfc.nasa.gov.

Stoneking, E. (2018). 42: An Open-Source Simulation Tool for Study and Design of Spacecraft Attitude Control Systems. *NASA Technical Reports Server (NTRS)*. https://ntrs.nasa.gov/citations/20180000954

United States Coast Guard (2024). L Band Antenna Panel Patterns and Performance. https://navcen.uscg.gov/lband-antenna-panel-patterns-and-performance

Winternitz, L. B., Bamford, W. A., Price, S. R., Carpenter J. R., Long, A. C., & Farahmand, M. (2017). Global Positioning System Navigation Above 76,000 km for NASA's Magnetospheric Multiscale Mission. *NAVIGATION, Volume: 64 Issue: 2, 289-300.*

Winternitz, Luke B., et al. "GPS based autonomous navigation study for the lunar gateway." *Annual American Astronautical Society (AAS) Guidance, Navigation, and Control Conference*. No. AAS 19-096. 2019.